PAPER

Check for updates

Preparation of Gd-doped AuNBP@mSiO$_2$ nanocomposites for the MR imaging, drug delivery and chemo-photothermal synergistic killing of breast cancer cells†

Shiyi Tang,[a] Ruohan Li,[ab] Tao Luo,[a] Tianhao Huang,[a] Xiaotong Lu,[a] Xinyao Wu,[a] Yulin Dong,[a] Changyu Wu, [ID][a] Kai Xu*[ab] and Yong Wang [ID]*[ab]

Under near-infrared (NIR) light, gold nanobipyramids (AuNBPs) exhibit a high photothermal conversion rate and photothermal stability, making them ideal mediators for photothermal therapy (PTT). In this study, highly purified AuNBPs are prepared, followed by coating their surfaces with mesoporous silica (mSiO$_2$). The obtained AuNBP@mSiO$_2$ nanocomplex exhibits an ellipsoidal shape with a relatively large specific surface, pore diameter and pore volume. To achieve MRI guided chemo-photothermal therapy of breast cancer cells, the nanocomplex is further coupled with the MRI contrast agent Gd-DTTA and the chemotherapeutic drug doxorubicin (DOX). The results indicated that under NIR light irradiation, AuNBPs exhibited promising PTT effects, while the cumulative release rate of DOX was significantly enhanced to 81.40%. Moreover, the chemo-photothermal therapy approach effectively eradicated 4T1 breast cancer cells. This work successfully confirms that chemo-photothermal synergistic therapy is an effective tumor treatment strategy and demonstrates the potential application of AuNBP@mSiO$_2$ as a nano-drug delivery platform. Additionally, it introduces new ideas for the integrated study of breast cancer diagnosis and treatment.

Introduction

In the past decades, cancers have been considered as a primary threat to human health.[1] Currently, surgery, radiotherapy, chemotherapy and endocrine therapy are major clinical approaches used in the treatment of various cancers.[2,3] However, the actual treatment efficacy is still limited due to the low specificity and severe side effects of these methods. For example, most drugs are poor in water solubility, high in metabolic turnover, and insufficient in targeting tumor cells in the postoperative adjuvant chemotherapy, resulting in systemic adverse reactions, damage to healthy normal tissues and the development of drug resistance in tumors.[4,5] Fortunately, nanotechnology has proposed a novel methodology to address the problems faced by the traditional treatment approaches. At this point, versatile multifunctional materials have been developed for precise imaging, surgical navigation, radiosensitivity enhancement, drug delivery and phototherapy (PTT), and *etc.*[6-8]

As an emerging therapeutic modality, PTT kills tumor cells by using a photothermal reagent, that converts light into heat when exposed to NIR. It shows great value in cancer treatment and controlled drug release due to its non-invasive nature, minimal damage to normal tissues and other advantages compared to traditional therapeutic methods.[8,9] Currently, various NIR laser absorbing nanomaterials were proposed to improve the photothermal conversion efficiency of PTT, including carbon nanomaterials, semiconductor nanoparticles and gold nanostructures.[10-12] Among these materials, gold-based nanomaterials have been widely investigated, such as nanorods, nanostars, nanocages and nanoshells, and *etc.*[10,13-15] Compared with other shapes of Au nanomaterials, AuNBPs, a novel type of Au nanostructures with two sharp tips, have attracted great attentions owing to their stronger and narrower localized surface plasmon resonance (LSPR) and photo-stability.[16] The strong NIR absorption capability makes the Au NBPs a promising mediator for PTT.[17-19]

Mesoporous silica nanoparticles (mSiO$_2$) are considered ideal drug nanocarriers and have been approved by the FDA for clinical trials in cancer treatment and imaging applications. Due to their stable skeleton structure, easy-to-modify inner and outer surfaces, large surface area, adjustable pore volume and low physiological toxicity, mSiO$_2$ can load drugs into its pores and achieve a controlled-release effect to improve drug durability.[20,21] Moreover, the surface of mSiO$_2$ is easily to be modified

[a] School of Medical Imaging, Xuzhou Medical University, Xuzhou, Jiangsu 221004, China. E-mail: wangyong@xzhmu.edu.cn; xkpaper@163.com

[b] Department of Radiology, Affiliated Hospital of Xuzhou Medical University, Xuzhou, Jiangsu 221002, China

with functional groups, providing it with multifunctionality. Furthermore, combining chemotherapy and PTT can further improve the therapeutic effect, including overcoming the resistance of tumor cells and reducing the adverse effects of chemotherapy drugs. To achieve this, $mSiO_2$ nanolayers can be coated on the surfaces of AuNBPs to obtain $AuNBP@mSiO_2$ nanocomposites, which offer high PTT efficiency and drug loading rate.

Magnetic resonance imaging (MRI) plays a crucial role in the precise diagnosis of cancers among other diagnostic methods such as fluorescence imaging, computer tomography (CT), ultrasounds, positron emission tomography (PET), and *etc.* This is due to its high resolution of soft tissue, lack of radiation damage, and the ability to conduct multi-sequence, multi-parameter, and multi-azimuth imaging.[22,23] However, currently used MRI contrast agents are mainly small molecule gadolinium chelates that lack sensitivity and often do not provide satisfactory image contrast enhancement in early disease stages. Previous studies have indicated that Gd^{3+}-chelates loaded silica nanoparticles exhibit highly enhanced T_1 MR relaxivity.[24,25] Hence, it is desirable to modify $mSiO_2$ with gadolinium chelates to enhance the MRI signal intensities.

In this study, we prepared $mSiO_2$ coated AuNBP ($AuNBP@mSiO_2$) with a core–shell structure. Then, we modified the surface with the Gd^{3+} chelated 3-amino-propyl(trimethoxysilyl)diethylenetriamine tetraacetic acid (Si-DTTA), a type of MRI contrast agent. Subsequently, we loaded the nanoprobes with DOX, resulting in the development of $AuNBP@mSiO_2$-Gd-DTTA@DOX. This integration allowed for MRI and chemo-photothermal killing of breast cancer cells. The findings of work provide a relevant research basis for the diagnosis, evaluation, and treatment of cancers.

Experimental

Reagents and materials

Gold chloride trihydrate ($HAuCl_4 \cdot 3H_2O$, 99.9%), sodium borohydride ($NaBH_4$, 98%), trisodium citrate (99.5%), gadolinium chloride ($GdCl_3$, 99%), hydrochloric acid (HCl, 36.0–38.0%), nitric acid (HNO_3, 65.0–68.0%), silver nitrate ($AgNO_3$, 99.8%), L-ascorbic acid (99.7%), sodium hydroxide (NaOH, 96.0%), cyclohexane (99.7%), tetraethyl orthosilicate and ethanol absolute (C_2H_6O, 99.7%) were purchased from Sinopharm Chemical Reagent Co., Ltd (Shanghai, China). Triethanolamine (TEA, AR), bromoacetic acid (AR), hexadecyltrimethylammonium bromide (CTAB, 99%) and cetyltrimethylammonium (CTAC, 97%) were bought from Aladdin Bio-Chem Technology Co., Ltd. (Shanghai, China). 3-(Trimethoxysilylpropyl)diethylene triamine was purchased from Gelest (Morrisville, US). Fetal bovine serum (FBS, Gibco), phosphate buffered saline (PBS), trypsin–EDTA and Dulbecco's modified Eagle medium (DMEM) were obtained from Beyotime Biotechnology (Nantong, China).

Preparation of AuNBP@mSiO₂-Gd-DTTA

Preparation of AuNBP. The procedure for the synthesis of AuNBP, as described in the ref. 26 and 27, began with the initial preparation of Au nanocrystal seeds. In a flask containing 9.625 mL of deionized water, 125 μL of 0.01 M $HAuCl_4$ solution and 250 μL of 0.01 M trisodium citrate solution were added while continuously stirring. Next, 150 μL of 0.01 M $NaBH_4$ solution, freshly prepared and cooled at 4 °C, was rapidly poured in with vigorous stirring. After stirring for 2 min, the mixture was allowed to stand undisturbed in a water bath at 25 °C for 2 h.

The AuNBP growth solution was then prepared as follows: 200 mL of 0.1 M CTAB was added to a clean and dry flask, followed by sequentially adding 10 mL of 0.01 M $HAuCl_4$, 2 mL of 0.01 M $AgNO_3$, 4 mL of 1 M HCl and 1.6 mL of 0.1 M ascorbic acid with continuously stirring. Then 1.46 mL of Au nanocrystal seeds solution was added under gentle stirring for 10 s, and left in a water bath at 25 °C for 12 h. The purification of AuNBP is a crucial step in the process. To initiate the growth of silver nanorods from AuNBP, the AuNBP growth solution underwent centrifugation at 8000 rpm for 15 min. The resulting precipitate was then dispersed in 160 mL of 0.08 M CTAC solution, using sonication. Subsequently, 16 mL of 0.01 M $AgNO_3$ solution and 8 mL of 0.1 mol L^{-1} ascorbic acid solution were added to the solution with stirring. The Ag nanorods were grown on the AuNBP surface by letting the solution stand at 65 °C for 4 h, after which the solution was naturally cooled to room temperature and centrifuged to remove the supernatant. The precipitate was further dispersed in 160 mL of 0.05 M CTAB solution and left to stand at room temperature for several days. The precipitates obtained in the reaction solution were AuNBP with Ag nanorods.

Next, the Ag nanorods on the AuNBP surface were etched away. The precipitated AuNBP with Ag nanorods was dispersed in 100 mL of deionized water, followed by the gentle addition of 2.5 mL of ammonia and 2 mL of hydrogen peroxide with stirring. The solution was allowed to stand while monitoring the etching process of Ag nanorods from the surface of AuNBP by UV-vis absorption. After complete etching, the solution was centrifuged and the precipitate was dispersed in 50 mL of CTAB solution with a concentration of 2 mM and stored at 4 °C for further use.

Preparation of AuNBP@mSiO₂. To encapsulate AuNBP with $mSiO_2$, a biphasic method was employed. Firstly, 24 mL of 25% CTAC solution and 180 μL of TEA were added to 36 mL of deionized water and stirred at 60 °C for 1 h. Next, a 5% cyclohexane solution of TEOS was slowly added, and the reaction was carried out at 60 °C for 12 h. The reaction solution was then centrifuged at 10 000 rpm for 15 min and the precipitate was washed in a 1% NaCl methanol solution, followed by repeated washing with ethanol. This step was taken to remove the template molecules, *i.e.*, CTAC, which act as pore-making agents in the encapsulation process of AuNBP with mesoporous $mSiO_2$.

Preparation of AuNBP@mSiO₂-Gd-DTTA. In the synthesis of the $AuNBP@mSiO_2$-Gd-DTTA nanocomplex, 0.5558 g of bromoacetic acid and 0.2654 g of 3-(trimethoxysilylpropyl)diethylene triamine were dissolved in a mixture of 1 mL of deionized water and 2 mL of 2 M NaOH solution with magnetic stirring for 10 min. The reaction solution was then heated to 50 °C, and

3 mL of 2 M NaOH solution was added dropwise, maintaining continuous stirring for 2 h at 50 °C. Following the reaction, the product solution was subjected to rotary evaporation to concentrate it, resulting in the formation of a yellow oily substance. Subsequently, this substrate was treated with ethanol, leading to the formation of a rice-white precipitate, identified as Si-DTTA. In the next step, 325.8 mg of Si-DTTA was dissolved in 12 mL of deionized water, and 1.14 mL of GdCl$_3$ solution (0.5 M) was added dropwise while stirring until the precipitate was no longer soluble. During this process, the pH value was adjusted to approximately 9 using 2 M NaOH solution. After 2 h, excess Gd^{3+} ions were removed using Chelex100, resulting in a 0.12 M Gd-Si-DTTA solution. Meanwhile, the previously prepared AuNBP@mSiO$_2$ was dispersed in ethanol, and a Gd-Si-DTTA solution along with ammonia was added to the mixture. The resulting solution was stirred at room temperature for 24 h and then subjected to centrifugation. The obtained precipitate was thoroughly washed multiple times with ethanol to obtain the final AuNBP@mSiO$_2$-Gd-DTTA nanocomplex.

Characterization of the nanocomplexes

Transmission electron microscopy (TEM) images were obtained using the JEM-200 EX transmission electron microscope (JEOL, Japan). For investigating the elements distribution, STEM equipped with EDS (Talos F200X, FEI, USA) was employed. The UV-Vis absorbance measurements were recorded using a UH-4150 spectrophotometer (Hitachi, Japan). Surface charges were analyzed using a Zetasizer Nano ZS90 equipment (Malvern Instruments Ltd, Malvern, UK). The specific surface area and pore size distribution of AuNBP@mSiO$_2$ were determined by performing BET tests using a TriStar II 3020 instrument (Micromeritics, USA). Furthermore, the gadolinium ion concentration in the AuNBP@mSiO$_2$-Gd-DTTA solution was measured using ICP-MS (Agilent ICPOES730, USA).

DOX loading and release

Preparation of AuNBP@mSiO$_2$-Gd-DTTA@DOX. DOX was loaded onto the surface of AuNBP@mSiO$_2$-Gd-DTTA following the protocol described in a previous report.[28] Specifically, 1 mg mL^{-1} of AuNBP@mSiO$_2$-Gd-DTTA was mixed with 1 mL of DOX at concentrations ranging from 25 to 400 μg mL^{-1}. The mixture was stirred at room temperature for 24 h in the dark. Subsequently, the resulting solutions were centrifuged at 10 000 rpm min^{-1} for 15 min, and this centrifugation step was repeated 3 times to effectively remove any free DOX from the solution.

DOX release form AuNBP@mSiO$_2$-Gd-DTTA@DOX. The release of DOX from AuNBP@mSiO$_2$-Gd-DTTA@DOX was investigated under different pH conditions, both in the presence and absence of NIR laser irradiation. The experimental procedure involved dispersing AuNBP@mSiO$_2$-Gd-DTTA@DOX in 2 mL of PBS buffer with varying pH values. Subsequently, the samples were subjected to 808 nm near-infrared light irradiation (at a power density of 1 W cm^{-2}) at 4 h and 12 h. The concentration of DOX released in each sample was determined using UV-Vis spectrophotometry with the standard curve method.

In vitro MRI performance

T$_1$ relaxivity evaluation of AuNBP@mSiO$_2$-Gd-DTTA. The AuNBP@mSiO$_2$-Gd-DTTA nanocomplex was dispersed in PBS at different concentrations of gadolinium ions, which were determined using the previously mentioned ICP-MS results. The T$_1$-weighted relaxation of AuNBP@mSiO$_2$-Gd-DTTA was measured using a 3.0T MRI scanner (Discovery 750w, GE, USA) with the following settings: T_E (echo time) = out of phase, T_R (repetition time) = 16.0 ms, matrix = 288 × 288, FOV (field of view) = 8 cm × 8 cm, and slice thickness = 1.0 mm.

MR imaging of cells with AuNBP@mSiO$_2$-Gd-DTTA. 4T1 breast cancer cells were cultured in a growth medium containing varying concentrations of AuNBP@mSiO$_2$-Gd-DTTA, ranging from 0.125 to 0.25 mg mL^{-1}. The cells were maintained in an incubator with 5% CO$_2$ at 37 °C for a duration of 6 h. After the incubation period, the culture medium was carefully removed, and the cells were washed three times with sterilized PBS to eliminate any excess nanocomplex. Next, the remaining cells were lysed with 0.25% trypsin, centrifuged and dispersed in 300 μL of sterilized PBS. MR images of the cells were obtained using the MRI scanner (Discovery 750w, GE, USA) to assess the cellular response to the AuNBP@mSiO$_2$-Gd-DTTA nanocomplex.

In vitro cytotoxicity of AuNBP@mSiO$_2$-Gd-DTTA

The *in vitro* cytotoxicity of AuNBP@mSiO$_2$-Gd-DTTA was assessed using the MTT assay. Both 4T1 breast cancer cells and 3T3 fibroblasts at logarithmic growth stage were seeded in a 96-well plate at a concentration of approximately 10^5 cells per mL. The cells were allowed grow until they covered the culture wells, as observed under an inverted microscope (IX51, Olympus, Japan). Subsequently, AuNBP@mSiO$_2$-Gd-DTTA solutions at various concentrations, ranging from 0 to 0.8 mg mL^{-1}, were added to the wells of the 96-well plate, resulting in a total volume in each well. After an additional 24 h of incubation, 100 μL of MTT solution was dispensed into each well, that had been rinsed twice with PBS, followed by an 4 h incubation. Next, the culture medium was removed, and 100 μL of DMSO was added to each well to dissolve the formazan crystals formed by viable cells. The optical density (OD) value of each well was measured at 490 nm using a microplate reader (BioTek Epoch, Service Card) to determine cell viability.

Photothermal efficiency

Thermal effect of nanocomplex. In the experiment, a total of 1 mL of deionized water, AuNBP solution, and AuNBP@mSiO$_2$-Gd-DTTA were added into each well of a 96-well plate. These samples were then subjected to irradiation using a NIR laser (FC-808-10W, Changchun New Industries Optoelectronics Technology Co. Ltd, Changchun, China) at different power intensities. To assess the temperature changes over time, a thermal imaging system (FLIR E60; FLIR Systems, Inc.,

Wilsonville, OR, USA) was applied to monitor temperature changes over time in each well during the irradiation period.

***In vitro* chemo-photothermal synergistic therapy of AuNBP@mSiO$_2$-Gd-DTTA@DOX.** 4T1 cells at the logarithmic growth stage were seeded in a 96-well culture plate at a concentration of approximately 5×10^4 cells per mL and incubated with 5% CO$_2$ at 37 °C for 24 h. After the incubation period, the growth medium was discarded, and the cells were washed twice with sterilized PBS. Subsequently, the cells were treated with different concentrations of AuNBP@mSiO$_2$-Gd-DTTA, AuNBP@mSiO$_2$-Gd-DTTA@DOX, DOX and PBS, respectively, using a total volume of 100 μL of growth medium. Following 48 h of incubation, some of the cells were exposed to NIR laser at a power density of 1 W cm^{-2} for 10 min. Subsequently, the cell viabilities for each group were evaluated using the MTT assay, as described previously. Additionally, to assess the synergistic therapeutic effect of the nanocomplex, calcein AM/PI staining was used to label live and dead cells. After treatment of nanocomplex and NIR irradiation, the cells cultured in Petri dishes (Φ 35 mm) were stained with calcein AM and PI, and then were imaged using a fluorescent microscope (IX51, Olympus, Japan) to determine the impact of the treatment on cell viability.

Results and discussion

Morphology and structure of AuNBP, AuNBP@mSiO$_2$ and AuNBP@mSiO$_2$-Gd-DTTA

Products during the fabrication process of AuNBP were characterized using TEM and UV-vis spectroscope. As shown in Fig. 1A, the AuNBP growth solution consisted of the mixture of Au nanoparticles and AuNBP, which exhibited two main absorption peaks at 550 nm and 815 nm (Fig. 1D). The size of Au nanoparticles was similar to that of AuNBP, making it challenging to separate them using conventional centrifugation methods. To address this, silver was grown onto the surface of both Au nanoparticles and AuNBP, resulting in the formation of core–shell Au/Ag nanoparticles and Au/Ag nanorods,

respectively, as evident from the TEM images (Fig. 1B) and the wide UV-Vis absorption band observed between 330–550 nm (Fig. 1D). The core–shell Au/Ag nanoparticles remained in the dispersive solution while the Au/Ag nanorods gradually precipitated when the mixture of core–shell Au/Ag nanoparticles and Au/Ag nanorods was left to stand for several days with dispersion in CTAB solution. After centrifugation, the Au/Ag nanorods were successfully separated, exhibiting a strong UV-Vis absorption peak at 380 nm, which corresponds to the transverse plasmon resonance absorption peak of Au/Ag nanorods, and a length of about 212 nm. As shown in Fig. 1C, it is evident that each AuNBP is enveloped in the middle of the Ag/Au nanorods.

Subsequently, pure AuNBP was obtained by etching the Au/Ag nanorods with ammonia and hydrogen peroxide to remove the silver from the two poles of AuNBP. As shown in Fig. 2A, the resulting AuNBP exhibited a bipyramid structure with a length of approximately 66.6 nm and a width of 24.9 nm. These findings provided evidence that well-dispersed and uniformly sized AuNBP were successfully fabricated. Furthermore, HRTEM (Fig. 2B) revealed the lattice fringes with a spacing of 0.22 nm, which corresponds to the {111} facets of face-centered-cubic (FCC) Au crystalline.[29,30]

To facilitate the loading of MR contrasts and chemotherapeutic agents, AuNBP was encapsulated with mesoporous silica. As shown in Fig. 2C, the resulting ellipsoid-like AuNBP@mSiO$_2$ exhibited excellent dispersion and uniform size, with a mesoporous silica shell approximately 30 nm in thickness. After the loading of Gd-Si-DTTA, AuNBP@mSiO$_2$-Gd-DTTA maintained its bipyramidal core and elliptical encapsulation structure, as observed in the TEM results (Fig. 2D). EDS mapping was utilized

Fig. 2 TEM images of AuNBP (A and B), AuNBP@mSiO$_2$ (C), and AuNBP@mSiO$_2$-Gd-DTTA (D). HAADF–STEM image (E) and EDS elemental mapping images of AuNBP@mSiO$_2$-Gd-DTTA (F–J): Au (F), Si (G), O (H), Gd (I), and overlap (J), respectively.
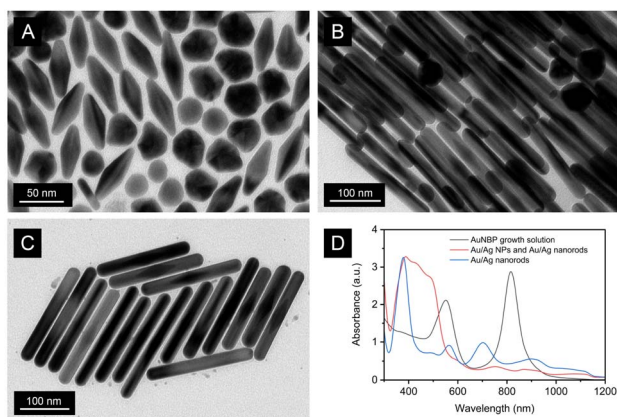
Fig. 1 TEM images of AuNBP growth solution (A), mixture of core–shell Au/Ag nanoparticles and Au/Ag nanorods (B), and Au/Ag nanorod dispersion (C), and UV-Vis absorption spectra of them (D).
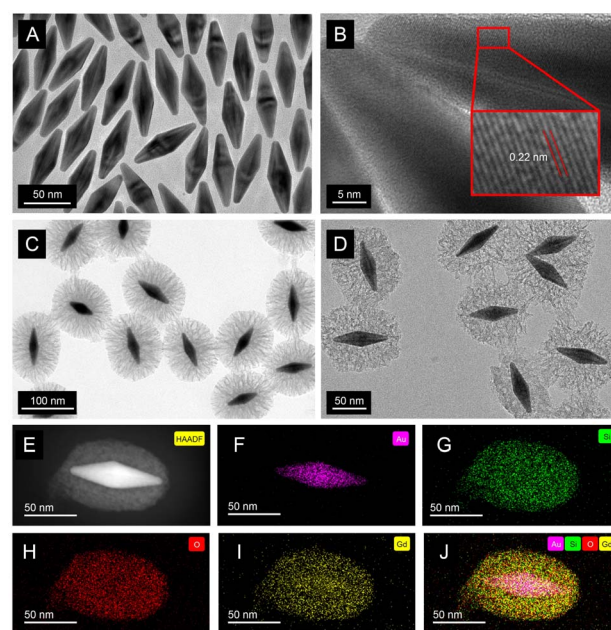
to analyze the elemental content and spatial distribution within AuNBP@mSiO$_2$-Gd-DTTA (Fig. 2E–J). The element Au was predominantly concentrated at the center of AuNBP@mSiO$_2$-Gd-DTTA, while Si, O, and Gd were distributed throughout the nanocomplex. As shown in Fig. 2E–J and Table S1,† the mass fraction of O, Si, Gd, and Au were 32.02, 15.42, 23.27, and 29.30 wt%, respectively.

The obtained results suggested that Gd-Si-DTTA has been successfully loaded onto the mesoporous AuNBP@mSiO$_2$, and the encapsulated AuNBP@mSiO$_2$-Gd-DTTA still retained sufficient pores, indicating promising potential for loading DOX, the chemotherapeutic agents.

Surface analysis of AuNBP@mSiO$_2$-Gd-DTTA@DOX

Fig. 3A and B depict the N$_2$ adsorption–desorption BET isotherm of AuNBP@mSiO$_2$. The pore size distribution for AuNBP@mSiO$_2$-Gd-DTTA ranged from 4 to 12 nm, with an average pore size of 9.5 nm. Additionally, the pore volume and specific surface area of AuNBP@mSiO$_2$-Gd-DTTA were measured to be 2.4 cm^3 g^{-1} and 961 m^2 g^{-1}, respectively. It is noteworthy that the average pore size, pore volume, and specific surface area achieved in this study are higher compared to most previous reports.[31,32]

The surface charges of the nanocomplexes were assessed as shown in the zeta potential diagram (Fig. 3C). The zeta potentials of AuNBP, AuNBP@mSiO$_2$ and AuNBP@mSiO$_2$-Gd-DTTA were about 26.7, −24.6 and −8.88 mV, respectively. Notably, DOX possesses a positively charged protonatable amino group. Therefore, the interaction between DOX and AuNBP@mSiO$_2$-Gd-DTTA resulted in the formation of AuNBP@mSiO$_2$-Gd-DTTA@DOX, as evidenced by the change in Zeta potential to 11.43 mV, confirming the successful loading of DOX within the mesoporous silicon pores.

The difference observed in the UV-Vis spectra lies in the absorption characteristics of AuNBP@mSiO$_2$-Gd-DTTA compared with AuNBP and AuNBP@mSiO$_2$ (Fig. 3D). AuNBP@mSiO$_2$-Gd-DTTA exhibited a prominent absorption peak at 817 nm, which was redshifted in comparison to AuNBP and AuNBP@mSiO$_2$, attributed to the successful loading of Gd-DTTA onto the nanocomplex. The adsorption peak at 500 nm of AuNBP@mSiO$_2$-Gd-DTTA@DOX was attributed to DOX. The redshift of adsorption peak at 834 nm for AuNBP@mSiO$_2$-Gd-DTTA@DOX can be attributed to the specific chromophore and auxochrome structures of DOX. Thus, the UV-Vis serve as the evidence supporting the successful loading of DOX onto AuNBP@mSiO$_2$-Gd-DTTA.

DOX loading and release with AuNBP@mSiO$_2$-Gd-DTTA

The optimization of DOX loading with AuNBP@mSiO$_2$-Gd-DTTA was depicted in Fig. 4A. The encapsulation efficiency and loading rate were found to reach their peak values of 74.03% and 56.30%, respectively, when the DOX concentration was set as 200 μg mL^{-1} and the pH level was maintained at 7.4. Based on these results, the condition of 200 μg mL^{-1} DOX concentration and pH 7.4 was selected as the optimal condition for DOX loading with AuNBP@mSiO$_2$-Gd-DTTA for the subsequent experiments.

Fig. 4B illustrates the release profile of DOX from AuNBP@mSiO$_2$-Gd-DTTA@DOX under neutral and acidic conditions, both in the presence and absence of NIR laser irradiation. Notably, AuNBP@mSiO$_2$-Gd-DTTA@DOX exhibited a slow release rate of 27.95% at pH 7.4 after 24 h. In contrast, a relatively higher release rate of 45.46% was observed at pH 5.3 during the same period. Moreover, the release rate was significantly increased when NIR laser irradiation was applied. Specifically, the total release of DOX from AuNBP@mSiO$_2$-Gd-DTTA@DOX reached 81.40% at pH 5.3 after undergoing two NIR irradiation cycles at 4 and 12 h. These findings demonstrate that NIR irradiation under acidic conditions can expedite the release of DOX from AuNBP@mSiO$_2$-Gd-DTTA@DOX, showcasing its potential for controlled drug release at specific sites, such as tumors.

T$_1$ MR performance of AuNBP@mSiO$_2$-Gd-DTTA

The concentration of gadolinium ions within AuNBP@mSiO$_2$-Gd-DTTA measured by ICP-MS was 0.123 mM (corresponding to 19.34 wt%, the results was shown in Table S2†). The T$_1$ MR performance of AuNBP@mSiO$_2$-Gd-DTTA was showed in Fig. 5. With the increasing concentration of gadolinium ions, the T$_1$ signal gradually increased, and the pseudo-colored T$_1$ map changed from dark blue to red-yellow in sync (Fig. 6A). The T$_1$
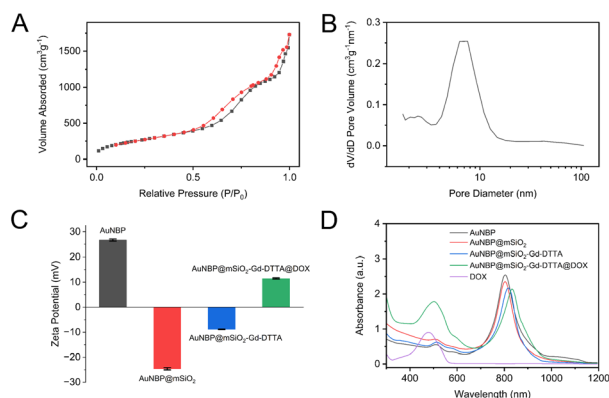

Fig. 3 (A) The N$_2$ adsorption–desorption BET isotherm of AuNBP@mSiO$_2$. (B) The distribution plot of pore sizes. (C) Zeta potential diagrams and (D) UV-vis absorption spectra of AuNBP, AuNBP@ mSiO$_2$, AuNBP@mSiO$_2$-Gd-DTTA and AuNBP@mSiO$_2$-Gd-DTTA@DOX.
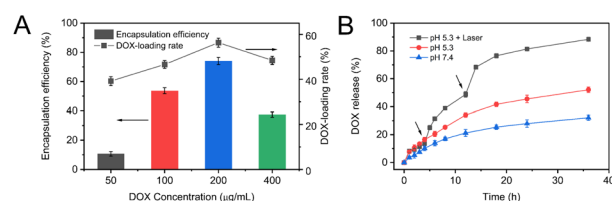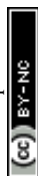

Fig. 4 (A) Encapsulation efficiency and loading rate of DOX for AuNBP@mSiO$_2$-Gd-DTTA. (B) DOX release from AuNBP@mSiO$_2$-Gd-DTTA@DOX under different pH values and NIR laser triggering conditions.
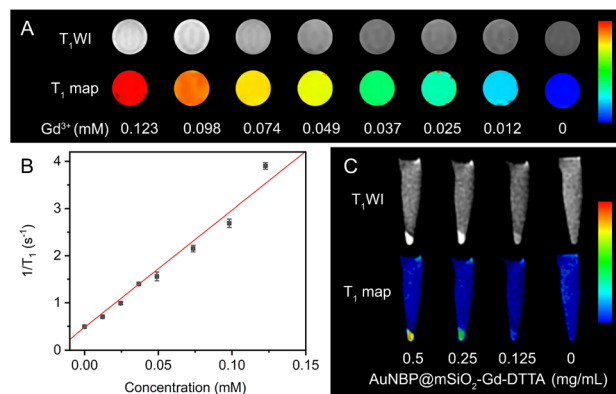
Fig. 5 (A) T_1WI and T_1 map of AuNBP@mSiO$_2$-Gd-DTTA *in vitro*. (B) Linear fit of T_1 relaxation time with the concentration of gadolinium ions. (C) T_1WI and T_1 map of 4T1 cells incubated with AuNBP@mSiO$_2$-Gd-DTTA of various concentrations. The bright-field image of cells in EP tube was shown in Fig. S1.†
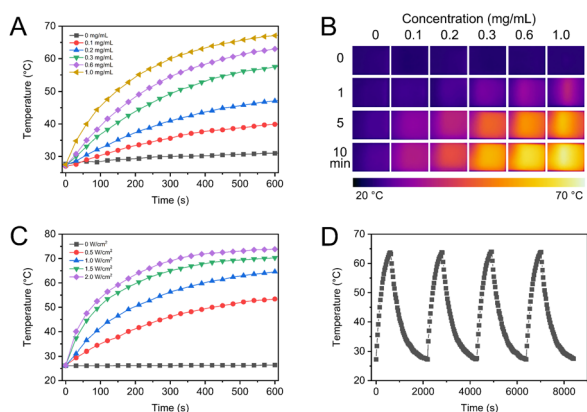

Fig. 6 (A) Photothermal temperature curves and (B) thermal images of AuNBP@mSiO$_2$-Gd-DTTA at different concentrations with a NIR laser irradiation (1.0 W cm^{-2}). (C) Photothermal temperature curves of AuNBP@mSiO$_2$-Gd-DTTA (0.6 mg mL^{-1}) under NIR laser irradiation with different powers. (D) Photothermal temperature curves of AuNBP@mSiO$_2$-Gd-DTTA (0.6 mg mL^{-1}) under laser ON/OFF cycles of NIR laser irradiation (1.0 W cm^{-2}).

relaxation rate (r_1) value of AuNBP@mSiO$_2$-Gd-DTTA, calculated from the slope of linear fit of T_1 relaxation time and concentration of gadolinium ions, was approximately 24.90 s^{-1} mM^{-1} (Fig. 6A), which was much higher than values reported in previously ref. 33 and 34.

As shown in Fig. 5, MR imaging of 4T1 breast cancer cells was successfully achieved. The T_1 imaging signals of 4T1 cells exhibited an increase with the rising concentration of AuNBP@mSiO$_2$-Gd-DTTA, as evident from the pseudo-colored T_1 map images. These findings suggest that AuNBP@mSiO$_2$-Gd-DTTA can serve as a contrast agent, enhancing the MR imaging of cells.

Photothermal effect of AuNBP@mSiO$_2$-Gd-DTTA

The photothermal effect of AuNBP@mSiO$_2$-Gd-DTTA at various concentrations was investigated under irradiation with an

808 nm NIR laser at different power intensities and irradiation times. As depicted in Fig. 6A and B, the PBS solution without AuNBP@mSiO$_2$-Gd-DTTA nanocomposites exhibited a minimal temperature increase of only 3.7 °C after 10 min of laser irradiation, indicating a negligible photothermal effect of PBS alone. However, upon NIR laser irradiation for 10 min, the temperature of AuNBP@mSiO$_2$-Gd-DTTA nanocomposites increased significantly by 14.8, 21.8, 32.4, 38.1 and 41.8 °C at concentrations of 0.1, 0.2, 0.3, 0.6 and 1.0 mg L^{-1}, respectively. This result indicated that AuNBP@mSiO$_2$-Gd-DTTA nanocomposites exhibit excellent photothermal conversion efficiency. According to previous reports,[35] cancer cells can be effectively killed through photothermal treatment when exposed to temperature above 45 °C for 5 min. Here, the temperature of AuNBP@mSiO$_2$-Gd-DTTA solution rapidly increased above 45 °C at low concentrations and power intensities. Moreover, the temperature elevation was directly proportional to the power intensities of the NIR laser (Fig. 6C).

Furthermore, the photothermal stability of AuNBP@mSiO$_2$-Gd-DTTA was investigated through several irradiation cycles of NIR laser on/off switches (Fig. 6D). After four repeated heating/cooling steps, the peak temperatures, reached by AuNBP with the irradiation of the NIR laser remained consistent, with a relative standard deviation (RSD) of 0.2%. These results demonstrated the excellent stability of AuNBP as a photothermal therapeutic application.

In vitro chemo-photothermal synergistic therapy of AuNBP@mSiO$_2$-Gd-DTTA@DOX

The cytotoxicity of AuNBP@mSiO$_2$-Gd-DTTA was evaluated using the MTT assay on 4T1 breast cancer cells and 3T3, as shown in Fig. 7A. Both cell types displayed robust growth, with cell viabilities of 96.1% and 95.8%, respectively, after 24 h of treatment with a high concentration of the nanocomplex (0.3 mg mL^{-1}). The cytotoxicity test revealed that AuNBP@mSiO$_2$-Gd-DTTA exhibited excellent biocompatibility with both tumor and normal cells *in vitro*, and there were no statistically significant differences ($P > 0.05$).

The *in vitro* chemo-photothermal synergistic therapeutic effects of AuNBP@mSiO$_2$-Gd-DTTA@DOX (250 μg mL^{-1}) on 4T1 cells were assessed using the MTT method. As shown in Fig. 7B, the cell survival rates for the control group and AuNBP@mSiO$_2$-Gd-DTTA without NIR laser irradiation were both above 90%. Treatment with DOX (11.4 μg mL^{-1}) with or without NIR laser
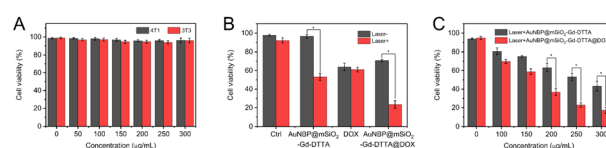

Fig. 7 (A) Cytotoxicity of AuNBP@mSiO$_2$-Gd-DTTA for 4T1 breast cancer cells and 3T3 fibroblasts. (B) Cell viability of 4T1 cells treated with different nanocomplex with and without NIR laser irradiation. (C) Cell viability of 4T1 cells under laser irradiation with different concentrations of AuNBP@mSiO$_2$-Gd-DTTA and AuNBP@mSiO$_2$-Gd-DTTA@DOX.
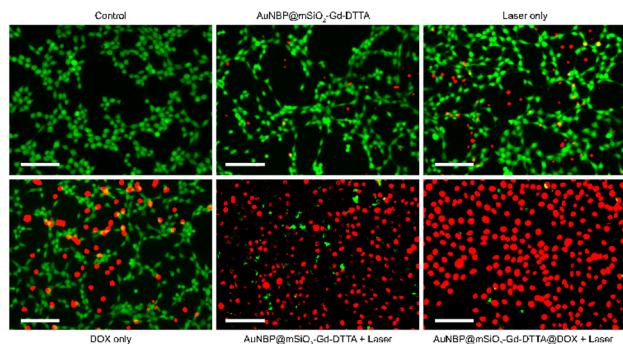
Fig. 8 Live/dead cell viability images of 4T1 cells treated with different nanocomplex (250 mg mL^{-1}) with/without NIR laser irradiation (scale bar 100 μm).

irradiation, resulted in an about 40% cell killing efficiency. In contrast, AuNBP@mSiO$_2$-Gd-DTTA and AuNBP@mSiO$_2$-Gd-DTTA@DOX with NIR laser irradiation induced an additional 43% and 47% cell mortality rate in tumor cells, respectively, which was statistically significant ($P < 0.05$).

Meanwhile, for further investigate the chemo-photothermal synergistic therapeutic efficiency, various concentrations of AuNBP@mSiO$_2$-Gd-DTTA and AuNBP@mSiO$_2$-Gd-DTTA@DOX along with NIR laser irradiation were applied to treat 4T1 cells, as represented in Fig. 7C. The cell viabilities were highly concentration-dependent and could decrease to 17.1% for 0.3 mg mL^{-1} of AuNBP@mSiO$_2$-Gd-DTTA@DOX with NIR laser irradiation. When the concentrations of the nanocomplex were higher than 0.3 mg mL^{-1}, there were statistically significant differences ($P < 0.05$) between AuNBP@mSiO$_2$-Gd-DTTA and AuNBP@mSiO$_2$-Gd-DTTA@DOX.

Furthermore, the synergistic effect was also investigated using the live/dead staining method (Fig. 8). Cells in the control group (with/without NIR laser irradiation) and the AuNBP@mSiO$_2$-Gd-DTTA group (without NIR laser irradiation) were mostly labeled with green, indicating that the cells remained in good condition with high viability. For the DOX only group, nearly half of the cells were labeled with green, suggesting the cell viability was above 60%, which is consistent with the above results. In contrast, for the AuNBP@mSiO$_2$-Gd-DTTA with NIR laser irradiation group, only a fraction of cells were labeled with green, while all cells were labeled with red for the AuNBP@mSiO$_2$-Gd-DTTA@DOX with NIR laser irradiation group. These results collectively demonstrated that AuNBP@mSiO$_2$-Gd-DTTA@DOX exhibited a significant chemo-photothermal synergistic effect for tumor treatment.

Indeed, the results suggest that AuNBP@mSiO$_2$-Gd-DTTA, loaded with DOX, combined with NIR laser irradiation, exerted a pronounced synergistic therapeutic effect on 4T1 cells, leading to enhanced therapeutic efficacy and potential applications in cancer therapy.

Conclusions

In this study, we designed a core–shell structured nanocomplex by using AuNBP with excellent photothermal effect as the core

and mSiO$_2$ as the shell. Further modification with Gd-Si-DTTA allowed us to obtain AuNBP@mSiO$_2$-Gd-DTTA, which demonstrated good biocompatibility, excellent photothermal conversion efficiency, and a high T$_1$ relaxation rate for MR imaging. The loading of DOX onto AuNBP@mSiO$_2$-Gd-DTTA resulted in AuNBP@mSiO$_2$-Gd-DTTA@DOX, which exhibited a high DOX loading rate, and demonstrated pH-sensitive and NIR laser-triggered DOX release. Remarkably, this nanocomplex showed a significant improvement in synergistic therapeutic effect by combining DOX-induced chemotherapy and AuNBP-induced photothermal therapy. This approach holds great promise for MR imaging guided cancer treatment with synergistic chemo-photothermal therapy *in vivo*.

Author contributions

Shiyi Tang: investigation, data curation, writing – original draft preparation, funding acquisition. Ruohan Li: investigation, data curation. Tao Luo: investigation, data curation, validation. Tianhao Huang: investigation, data curation, funding acquisition. Xiaotong Lu: investigation, data curation, funding acquisition. Xinyao Wu: data curation, funding acquisition. Yulin Dong: data curation, funding acquisition. Changyu Wu: visualization, writing – original draft preparation, validation. Kai Xu: funding acquisition, project administration. Yong Wang: conceptualization, methodology, writing – reviewing and editing.

Conflicts of interest

There are no conflicts to declare.

Acknowledgements

Notes and references

1 R. L. Siegel, K. D. Miller, N. S. Wagle and A. Jemal, *Ca-Cancer J. Clin.*, 2023, **73**, 17–48.

2 J. Zugazagoitia, C. Guedes, S. Ponce, I. Ferrer, S. Molina-Pinelo and L. Paz-Ares, *Clin. Ther.*, 2016, **38**, 1551–1566.

3 A. G. Waks and E. P. Winer, *JAMA, J. Am. Med. Assoc.*, 2019, **321**, 288–300.

4 W. Zhou, T. Pan, H. Cui, Z. Zhao, P. K. Chu and X.-F. Yu, *Angew. Chem., Int. Ed.*, 2019, **58**, 769–774.

5 E. F. Blackley and S. Loi, *Breast*, 2019, **48**(Suppl 1), S44–S48.

6 V. Jain, H. Kumar, H. V. Anod, P. Chand, N. V. Gupta, S. Dey and S. S. Kesharwani, *J. Controlled Release*, 2020, **326**, 628–647.

7 L. N. Borgheti-Cardoso, J. S. R. Viegas, A. V. P. Silvestrini, A. L. Caron, F. G. Praça, M. Kravicz and M. V. L. B. Bentley, *Adv. Drug Delivery Rev.*, 2020, **153**, 109–136.

8   B. Nasseri, E. Alizadeh, F. Bani, S. Davaran, A. Akbarzadeh, N. Rabiee, A. Bahadori, M. Ziaei, M. Bagherzadeh, M. R. Saeb, M. Mozafari and M. R. Hamblin, *Appl. Phys. Rev.*, 2022, **9**, 011317.

9   X. Li, J. F. Lovell, J. Yoon and X. Chen, *Nat. Rev. Clin. Oncol.*, 2020, **17**, 657–674.

10 X. Luo, B. Zhang, Y. Zhang, Z. Meng, P. Li, X. Jiang, J. Xiao, C. Lin and W. Su, *Photodiagn. Photodyn. Ther.*, 2022, **39**, 102988.

11 H. Shi, R. Yan, L. Wu, Y. Sun, S. Liu, Z. Zhou, J. He and D. Ye, *Acta Biomater.*, 2018, **72**, 256–265.

12 S. Feng, J. Lu, K. Wang, D. Di, Z. Shi, Q. Zhao and S. Wang, *Chem. Eng. J.*, 2022, **435**, 134886.

13 D. Kalinowska, I. Grabowska-Jadach, M. Liwinska, M. Drozd, M. Pietrzak, A. Dybko and Z. Brzozka, *Biosens. Bioelectron.*, 2019, **126**, 214–221.

14 S. Wang, Y. Song, K. Cao, L. Zhang, X. Fang, F. Chen, S. Feng and F. Yan, *Acta Biomater.*, 2021, **134**, 621–632.

15 R.-T. Li, M. Chen, Z.-C. Yang, Y.-J. Chen, N.-H. Huang, W.-H. Chen, J. Chen and J.-X. Chen, *Nanoscale*, 2022, **14**, 9818–9831.

16 C. Fang, G. Zhao, Y. Xiao, J. Zhao, Z. Zhang and B. Geng, *Sci. Rep.*, 2016, **6**, 36706.

17 T. H. Chow, N. Li, X. Bai, X. Zhuo, L. Shao and J. Wang, *Acc. Chem. Res.*, 2019, **52**, 2136–2146.

18 W. Rao, Q. Li, Y. Wang, T. Li and L. Wu, *ACS Nano*, 2015, **9**, 2783–2791.

19 C. Li, E. Mei, C. Chen, Y. Li, B. Nugasur, L. Hou, X. Ding, M. Hu, Y. Zhang, Z. Su, J. Lin, Y. Yang, P. Huang and Z. Li, *ACS Appl. Mater. Interfaces*, 2020, **12**, 12541–12548.

20 C. Mo, L. Lu, D. Liu and K. Wei, *J. Nanobiotechnol.*, 2020, **18**, 55.

21 X. Li, X. Zhang, Y. Zhao and L. Sun, *J. Inorg. Biochem.*, 2020, **202**, 110887.

22 A. R. Padhani, J. Barentsz, G. Villeirs, A. B. Rosenkrantz, D. J. Margolis, B. Turkbey, H. C. Thoeny, F. Cornud, M. A. Haider, K. J. Macura, C. M. Tempany, S. Verma and J. C. Weinreb, *Radiology*, 2019, **292**, 464–474.

23 T. Anani, S. Rahmati, N. Sultana and A. E. David, *Theranostics*, 2021, **11**, 579–601.

24 W. J. Rieter, J. S. Kim, K. M. L. Taylor, H. An, W. Lin, T. Tarrant and W. Lin, *Angew. Chem., Int. Ed.*, 2007, **46**, 3680–3682.

25 K. M. L. Taylor, J. S. Kim, W. J. Rieter, H. An, W. Lin and W. Lin, *J. Am. Chem. Soc.*, 2008, **130**, 2154–2155.

26 Q. Li, X. Zhuo, S. Li, Q. Ruan, Q.-H. Xu and J. Wang, *Adv. Opt. Mater.*, 2015, **3**, 801–812.

27 J. Feng, L. Chen, Y. Xia, J. Xing, Z. Li, Q. Qian, Y. Wang, A. Wu, L. Zeng and Y. Zhou, *ACS Biomater. Sci. Eng.*, 2017, **3**, 608–618.

28 C. Xu, F. Chen, H. F. Valdovinos, D. Jiang, S. Goel, B. Yu, H. Sun, T. E. Barnhart, J. J. Moon and W. Cai, *Biomaterials*, 2018, **165**, 56–65.

29 X. Kou, W. Ni, C.-K. Tsung, K. Chan, H.-Q. Lin, G. D. Stucky and J. Wang, *Small*, 2007, **3**, 2103–2113.

30 A. Mehere and N. B. Chaure, *Appl. Phys. A*, 2020, **126**, 662.

31 S. Shen, H. Tang, X. Zhang, J. Ren, Z. Pang, D. Wang, H. Gao, Y. Qian, X. Jiang and W. Yang, *Biomaterials*, 2013, **34**, 3150–3158.

32 H. Tang, S. Shen, J. Guo, B. Chang, X. Jiang and W. Yang, *J. Mater. Chem.*, 2012, **22**, 16095–16103.

33 Y. Wang, M. Li, T. Luo, M. Jiao, S. Jin, P. Dou, F. Zuo, C. Wu, C. Han, J. Li, K. Xu and S. Zheng, *Mater. Sci. Eng., C*, 2021, **127**, 112190.

34 J. Li, J. You, Y. Dai, M. Shi, C. Han and K. Xu, *Anal. Chem.*, 2014, **86**, 11306–11311.

35 Z. Chen, Q. Wang, H. Wang, L. Zhang, G. Song, L. Song, J. Hu, H. Wang, J. Liu, M. Zhu and D. Zhao, *Adv. Mater.*, 2013, **25**, 2095–2100.